

One-Dimensional Assembly on Two-Dimensions: AuCN Nanowire Epitaxy on Graphene for Hybrid Phototransistors

Jeongsu Jang,[†] Yangjin Lee,[‡] Jun-Yeong Yoon,[‡] Hoon Hahn Yoon,[†] Jahyun Koo,[§] Jeongheon Choe,[‡] Sungho Jeon,^{||} Jongbaek Sung,^{⊥,#} Jungwon Park,^{⊥,#} Won Chul Lee,^{||} Hoonkyung Lee,[§] Hu Young Jeong,[▽] Kibog Park,[†] and Kwanpyo Kim^{*,‡,||}

[†]Department of Physics, Ulsan National Institute of Science and Technology (UNIST), Ulsan 44919, Korea

[‡]Department of Physics, Yonsei University, Seoul 03722, Korea

[§]Department of Physics, Konkuk University, Seoul 05029, Korea

^{||}Department of Mechanical Engineering, Hanyang University, Ansan 15588, Korea

[⊥]School of Chemical and Biological Engineering, Institute of Chemical Process, Seoul National University, Seoul 08826, Korea

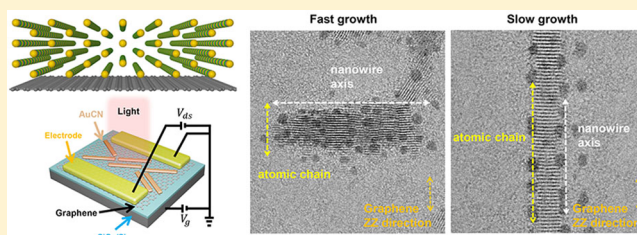
[#]Center for Nanoparticle Research, Institute for Basic Science (IBS), Seoul 08826, Korea

[▽]UNIST Central Research Facilities (UCRF), Ulsan National Institute of Science and Technology (UNIST), Ulsan 44919, Korea

Supporting Information

ABSTRACT: The van der Waals epitaxy of functional materials provides an interesting and efficient way to manipulate the electrical properties of various hybrid two-dimensional (2D) systems. Here we show the controlled epitaxial assembly of semiconducting one-dimensional (1D) atomic chains, AuCN, on graphene and investigate the electrical properties of 1D/2D van der Waals heterostructures. AuCN nanowire assembly is tuned by different growth conditions, although the epitaxial alignment between AuCN chains and graphene remains unchanged. The switching of the preferred nanowire growth axis indicates that diffusion kinetics affects the nanowire formation process. Semiconducting AuCN chains endow the 1D/2D hybrid system with a strong responsivity to photons with an energy above 2.7 eV, which is consistent with the bandgap of AuCN. A large UV response (responsivity $\sim 10^4$ A/W) was observed under illumination using 3.1 eV (400 nm) photons. Our study clearly demonstrates that 1D chain-structured semiconductors can play a crucial role as a component in multifunctional van der Waals heterostructures.

KEYWORDS: AuCN Nanowires, 1D/2D van der Waals heterostructures, phototransistors, 1D chain epitaxy



The switching of the preferred nanowire growth axis indicates that diffusion kinetics affects the nanowire formation process. Semiconducting AuCN chains endow the 1D/2D hybrid system with a strong responsivity to photons with an energy above 2.7 eV, which is consistent with the bandgap of AuCN. A large UV response (responsivity $\sim 10^4$ A/W) was observed under illumination using 3.1 eV (400 nm) photons. Our study clearly demonstrates that 1D chain-structured semiconductors can play a crucial role as a component in multifunctional van der Waals heterostructures.

Because of emerging properties originating from the interactions between different components, van der Waals heterostructures incorporating two-dimensional (2D) materials have been intensively studied for investigation of various fundamental physical and chemical properties as well as applications for next-generation electronic devices.^{1–3} For example, the interfaces between 2D layers can host interesting electronic bandstructure, charge carrier dynamics, and structural reconstruction originating from interlayer interaction.^{4–10} Organic molecular films and inorganic materials can also be interfaced with the 2D layers to form heterojunctions exhibiting synergetic electrical and optical properties suitable for high-performance transistors, photodetectors, photovoltaics, and light-emitting diodes.^{3,11–18}

The coherent interaction between components through relatively weak van der Waals forces is often undermined by surface dangling bonds or interface residue. Various 2D materials are naturally equipped with well-terminated surface, which makes them highly suitable for van der Waals vertical heterostructures. Similarly, inorganic 1D atomic chain

materials, possessing strong covalent bonds in axial directions and van der Waals-like interaction between the chains, can interact with 2D materials without any disturbance from dangling bonds. One such candidate is gold(I) cyanide (AuCN)¹⁹ which has the atomic structure of $(-\text{Au}-\text{C}\equiv\text{N}-)_n$. Previous studies have demonstrated the 1D/2D van der Waals heterostructure assembly (Figure 1a) through the epitaxial alignment of the 1D atomic chains of AuCN on graphene.^{20,21} However, the detailed assembly process of 1D chains on graphene or any synergetic properties arising from van der Waals interactions were not studied in the previous work, limiting the fundamental understanding of these 1D/2D hybrid systems and their applications.

In this study, we investigated the controlled fabrication and synergetic operation of a 1D/2D van der Waals heterostructure formed with AuCN and graphene. First, we examined in detail

Received: June 4, 2018

Revised: September 18, 2018

Published: September 24, 2018

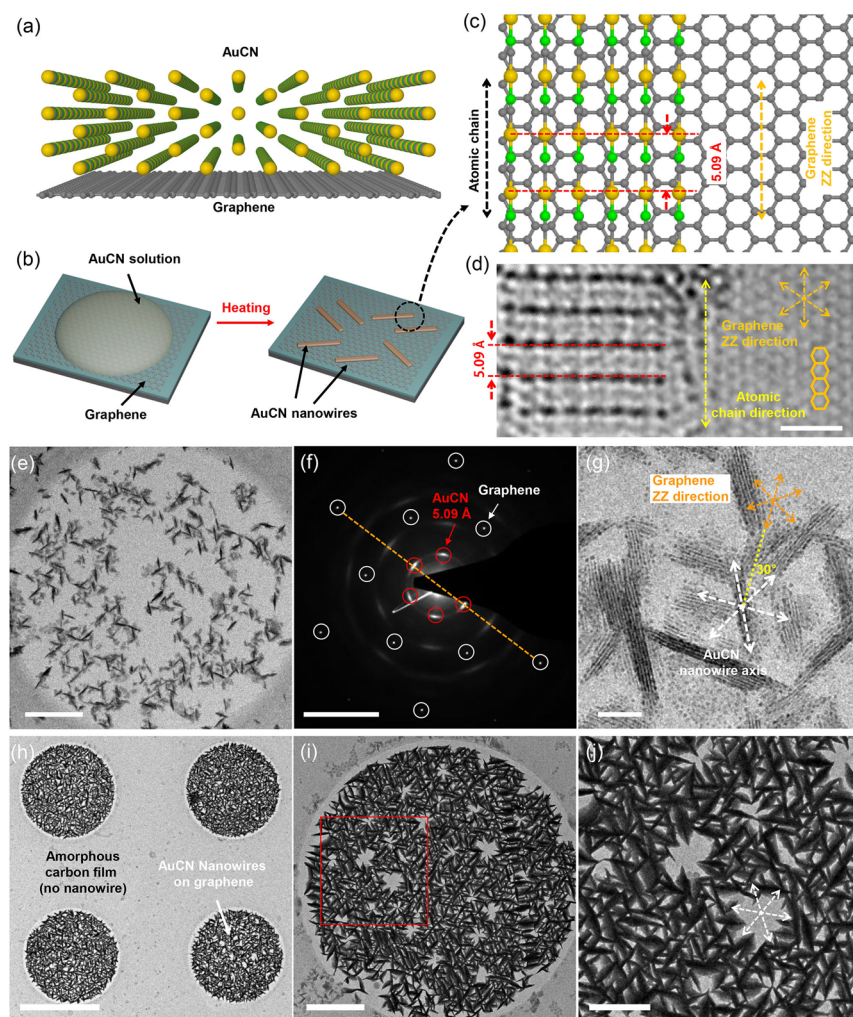


Figure 1. Epitaxially aligned AuCN nanowires on graphene. (a) Schematic of 1D AuCN atomic chains on graphene. (b) Schematic of AuCN nanowire growth process. (c) Atomic model of AuCN on graphene. (d) High-resolution TEM image of AuCN on graphene. Scale bar, 1 nm. (e) TEM image of synthesized AuCN nanowires on graphene using a 0.8 mM AuCN solution. Scale bar, 250 nm. (f) SAED of AuCN on graphene. Scale bar, 5 nm^{-1} . (g) Magnified TEM image of AuCN nanowires on graphene. Scale bar, 50 nm. (h–j) TEM image of synthesized AuCN nanowires on graphene using a 2.0 mM AuCN solution. Scale bar, $2 \mu\text{m}$, 500 nm, 200 nm, respectively. The red box in panel i is the field of view for panel j.

the growth behaviors of 1D semiconducting AuCN atomic chains on graphene using transmission electron microscopy (TEM). Although 1D AuCN atomic chains always align along with the zigzag lattice of the underlying graphene substrate, the nanowire assembly of 1D chains shows that their morphology changes depending on the growth conditions. We found that the nanowire axis is perpendicular to the molecular chain axis when a fast drop-cast method was used due to diffusion kinetics. In contrast, the nanowire morphology was parallel to the molecular chain axis when a slow incubation method was used. Second, we investigated the optoelectronic properties and phototransistor behaviors of the 1D/2D van der Waals heterostructure. Semiconducting AuCN chains endowed the 1D/2D heterostructures a strong responsivity to photons with an energy above 2.7 eV, which is consistent with the bandstructure of AuCN. We observed a large UV response with a responsivity $\sim 10^4$ A/W under illumination of 3.1 eV (400 nm) photons.

Results and Discussion. To form epitaxially grown AuCN nanowires on graphene, a facile drop-cast method was utilized. Figure 1b shows the schematic illustration of the AuCN

nanowire growth process on a graphene substrate. In brief, AuCN-dissolved solutions with various AuCN concentrations were dropped onto single-layer chemical vapor-deposited (CVD) graphene samples (graphene on SiO_2/Si or graphene TEM grid) and dried under mild heating on a hot plate (see Methods for details). TEM imaging was utilized to investigate the detailed nanowire crystal structure and their alignment with respect to the graphene substrate. We found that the drop-cast method allows for the successful formation of AuCN nanowires on graphene (Figure 1c–j). At a 0.8 mM concentration, the scattered nanowires formed on graphene, where the three-fold nanowire directions were clearly observed (Figure 1e–g). Selected area electron diffraction (SAED) was also employed to study the overall directional alignment of AuCN on graphene as shown in Figure 1f. Observed AuCN diffraction peaks were positioned along the graphene zigzag directions, which indicates that the atomic chains of AuCN nanowires were preferentially aligned to the graphene zigzag lattice directions.²⁰ This observation was consistent with the high-resolution TEM images in Figure 1d.

The drop cast method has various advantages including the ability to control the density of the nanowires and to confine nanowire growth to graphene. By either controlling the concentration of AuCN or increasing the number of drop-casts, we demonstrated that the density of nanowires grown on graphene was controllable (Supporting Figure S1). When a high AuCN concentration (2.0 mM) was used, we observed that the nanowire formation almost fully covered the graphene surface (Figure 1h–j). As shown in Figure 1h, the nanowires also selectively grew on the graphene surface but did not grow on the amorphous carbon substrates. This selectivity was consistent with our previous observation, where AuCN spontaneously bonds to the graphene substrate.²⁰ The zoom-in image (Figure 1j) clearly shows the three-fold symmetric growth direction of nanowires (white dashed arrows). We caution that the excessive deposition (multiple droplets with 2.4 mM) may lead to formation of AuCN films rather than the epitaxial growth of AuCN on graphene (Supporting Figure S2).

A careful investigation of the nanowire morphology revealed that the nanowire formation process depends on the growth conditions. As shown in Figure 1d, we found that, although AuCN atomic chains were aligned to the graphene zigzag lattice (orange dashed arrows), AuCN nanowire axes (white dashed arrows) were in fact perpendicular to the atomic chain (Figure 1g). This was in contrast to previous observations where the AuCN nanowire axes were parallel to the atomic chain.^{20,21} We studied the evolution of the nanowire morphology under different growth conditions (Figure 2). With relatively high (≥ 0.8 mM) concentrations, the nanowire elongation on the graphene substrate was perpendicular to the graphene zigzag lattice (Figure 1g, Figure 2a, and Supporting Figure S3). On the other hand, the nanowire morphology showed that the preferred formation axis was parallel to the graphene zigzag lattice with low AuCN concentrations using the drop-cast method or with the incubation method (Figure 2b and Supporting Figure S3). Figure 2c–e clearly show the evolution of nanowire dimensions along the graphene zigzag lattice and armchair lattice directions together with their aspect ratio under different growth conditions.

The observed morphology evolution can be attributed to the competition between the kinetic factors and thermodynamic effect during the AuCN growth on graphene.^{22,23} With a very slow growth process, where the deposition rate of materials is smaller compared to the diffusion rate on the substrate, the crystal morphology is mainly governed by the thermodynamic effect, which drives the system toward the lowest energy configuration.^{22,23} On the other hand, with a fast growth process where the deposition rate is high the kinetic factors are crucial in determining the nanostructure formation. The incubation method is a very slow process and, therefore, the observed parallel configurations (nanowire axis in the direction of the zigzag lattice) with incubation are likely to be low energy configurations. The nanowire morphology with a longer axis in the direction of the atomic chain can be rationalized by the stronger covalent bond along the chain compared to the weaker van der Waals interaction across the chains. On the contrary, the perpendicular direction growth mode, observed with high concentration drop-cast process, can be explained by kinetic factors concerning the fast deposition rate compared to the diffusion rate of the molecular moiety on the graphene surface.

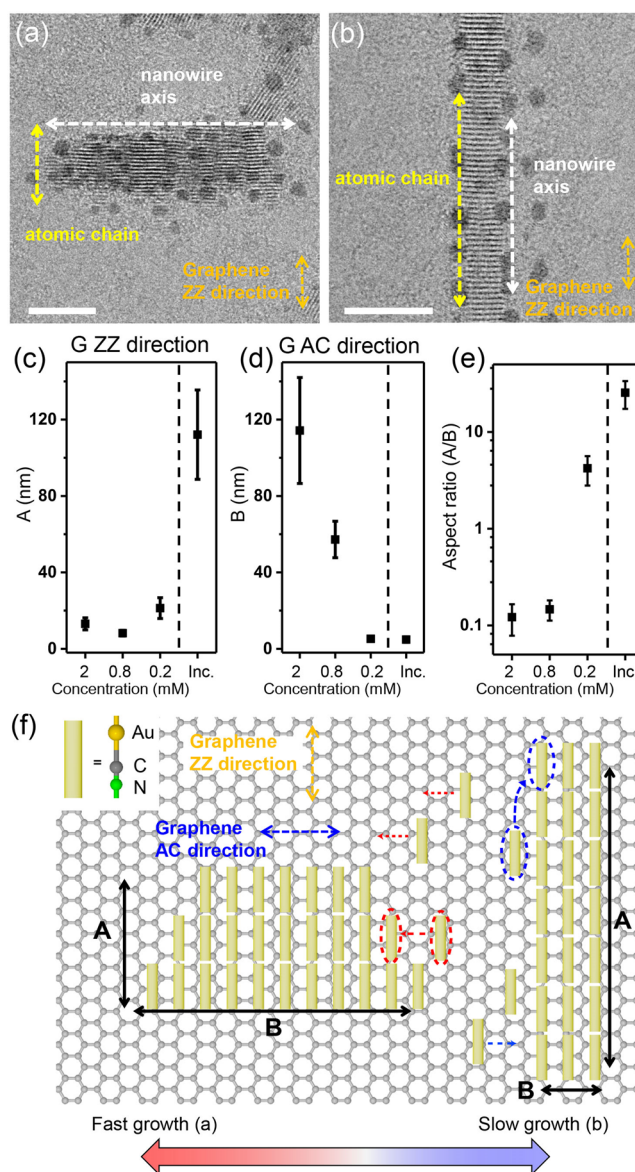


Figure 2. Evolution of AuCN nanowire morphology under different growth conditions. (a,b) TEM images of a synthesized AuCN nanowire on graphene (a) with a fast drop-cast process and (b) with a slow incubation method. Scale bar, 10 nm. (c) Dimension of nanowires in the direction of the graphene zigzag (ZZ) lattice. (d) Dimension of nanowires in the direction of the graphene armchair (AC) lattice. (e) Aspect ratio of nanowires. (f) Schematic illustration of different formation behaviors of AuCN nanowires on the graphene surface.

We now discuss the electrical properties of hybrid AuCN/graphene structures. There have been very limited number of research works²⁴ on the electrical and optical properties of AuCN prior to our work. We performed optical characterizations of AuCN together with its bandstructure calculations. Figure 3a shows the optical transmittance of the AuCN/graphene samples. With the deposition of AuCN on graphene, we observed a significant reduction in the transmittance with the appearance of a structure around the 450 nm wavelength. The transmittance data were converted to an absorption plot, which indicates that the estimated direct bandgap of AuCN is around 2.7–2.8 eV as shown in Figure 3b. The slight shift of absorption edge can be attributed to the different nanowire

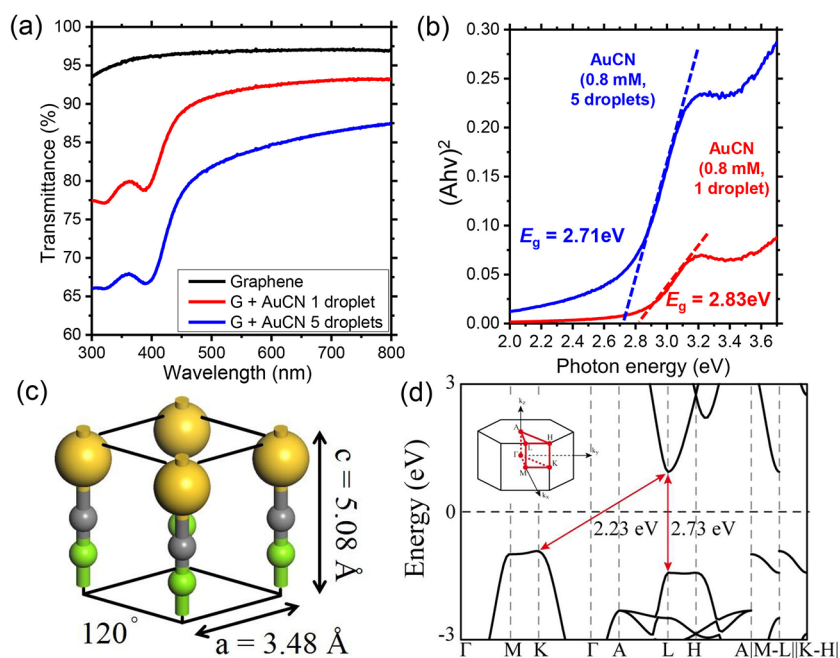


Figure 3. Optical absorption measurement and the bandstructure of AuCN. (a) Optical transmittance of graphene and AuCN/graphene samples. (b) Optical absorption plot as a function of photon energy. (c) AuCN crystal structure. (d) Calculated bandstructure of AuCN, where the Fermi level was set to zero. The inset shows the symmetric k-point paths in the Brillouin zone.

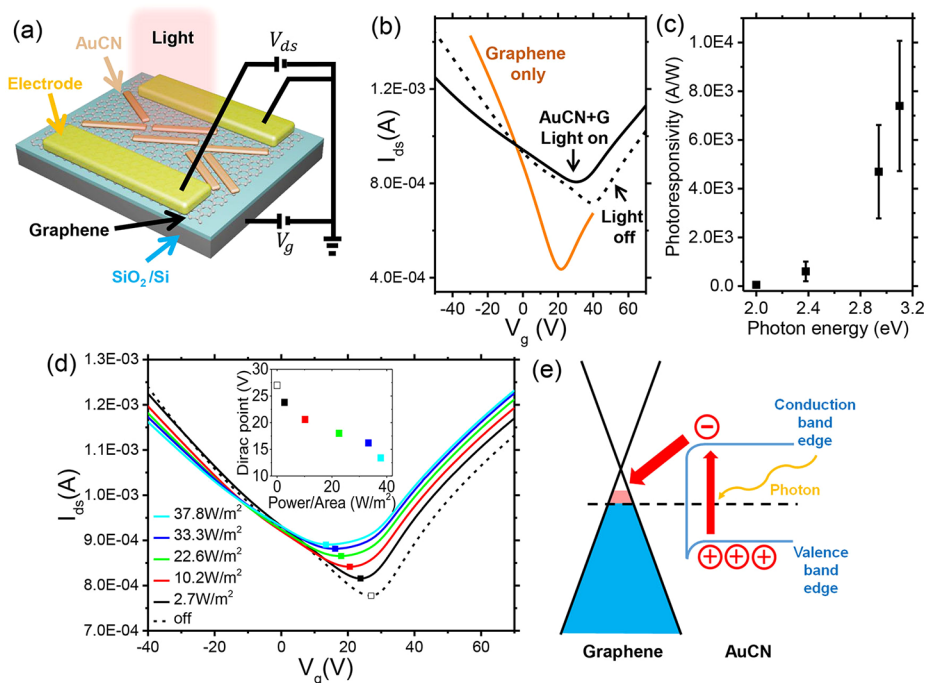


Figure 4. AuCN/graphene hybrid phototransistors. (a) Schematic of the AuCN/graphene field effect transistor. (b) Transfer curve of devices with $V_{ds} = 0.1\text{ V}$ (0.8 mM, 1 drop). The solid (dotted) black line is the response of the AuCN/G device with (without) light illumination. The orange line is obtained from a bare graphene device. (c) Photon-energy-dependent photoresponsivity of the AuCN/graphene device. (d) Transfer characteristics ($V_{ds} = 0.1\text{ V}$) of the AuCN/graphene device under different illumination powers. (e) Band alignment diagram at the interface between graphene and AuCN under the light illumination condition.

size and morphology depending on the AuCN deposition quantity on graphene. For the conversion of the transmittance data to absorption plots, we considered the possible scattering/reflectance changes from roughened surface of AuCN deposited samples. The measured difference in diffuse reflectance (Supporting Figure S4) was smaller than 1%

compared to graphene sample and the estimated values of AuCN bandgap were not affected when we considered the increased scattering.

We also performed density functional theory (DFT) calculations on the hexagonal bulk AuCN crystal (Figure 3c). The lattice constants of the AuCN crystal were calculated

to be 3.48 and 5.08 Å for the axial distance and height, respectively, which is in agreement with the experimental values of 3.40 and 5.09 Å.¹⁹ The calculated electronic bandstructure of the bulk AuCN obtained using the HSE method is shown in Figure 3d. The band structure shows that AuCN is a semiconductor with a direct bandgap of 2.73 eV and an indirect bandgap of 2.23 eV. The calculated value of the direct bandgap at L point is consistent with the experimentally observed value. The another band-to-band transition near H point is possible around 4.0 eV, which is consistent with the observed features in transmittance and absorption plots. We also observed that the calculated valence band along the M-K path and along the L-H path showed a very flat bandstructure. The M-K or L-H paths correspond to the perpendicular direction to the AuCN chain axis and the obtained flat bandstructure indicates that there is very weak electron-electron bonding between the AuCN chains.

To investigate the interaction between AuCN and graphene, we fabricated field effect transistor devices using the hybrid AuCN/graphene structure as shown in Figure 4a (see Methods and Supporting Figure S5 for details). The bare graphene devices on SiO₂/Si substrate showed usual ambipolar graphene transport characteristics with a minimum conduction point (Dirac point) around 20 V and a charge carrier mobility of ~ 1000 cm²/(V·s) under vacuum at room temperature. We observed that the bare graphene device did not show a photoresponse under light illumination, which is consistent with previous studies.^{25,26} The photogenerated carriers in graphene are not expected to yield photoconductance due to ultrafast (\sim ps) recombination in graphene.²⁷

After the formation of AuCN nanowires on graphene, the AuCN/graphene devices (0.8 mM, 1 drop) showed a change in the transfer curves. We generally observed reduced charge carrier mobility (~ 500 cm²/(V·s)) in addition to an upshift of Dirac point to 40 V after AuCN deposition on graphene (Figure 4b). The shift of Dirac point indicates that electrons are transferred from graphene to AuCN, which results in an increased p-doping of graphene due to the AuCN-graphene interaction. The polarity of charge transfer was consistent with previous calculations.²⁰ With the electron donation from graphene to AuCN, the AuCN band edge is expected to be bent downward at the interface (Figure 4e). Under the white light illumination, the AuCN/graphene device showed a large photoresponse as shown in Figure 3b. We also observed that the Dirac point was downshifted to ~ 30 V under illumination, which indicates that p-doping of graphene was reduced with incident photons compared to the light-off condition.

The main mechanism of the observed high photoresponse in the AuCN/graphene heterostructures can be explained by the photogating effect, which has been previously discussed in other graphene hybrid phototransistors.^{25,26,28} In the AuCN/graphene hybrid phototransistors, photogenerated holes and electrons in AuCN can be transferred to graphene with different transfer rate because of the built-in electric field at the AuCN-graphene interface.²⁸ Because of the unequal transfer rate between holes and electrons, there will be an extra charge-accumulation in AuCN, which results in the photogating effect. The photon-energy-dependent photoresponse of AuCN/graphene devices clearly shows that the device responsivity starts to rapidly increase around 2.7 eV, which is consistent with the measured direct bandgap value of AuCN (Figure 4c). With UV (3.1 eV) illumination, we observed a large photoresponsivity of ~ 8000 A/W and an external quantum

efficiency of $\sim 2 \times 10^4$ (Supporting Figure S6). The photoresponsivity of devices strongly depends on nanowire growth conditions and the increased photoresponsivity was generally observed with increased density of nanowires. The best performance ($\sim 3 \times 10^4$ A/W) was achieved with devices using drop-cast of 2.4 mM solution (Supporting Figure S7). The relatively large variation of photoresponsivity with 2.4 mM solution may be related to the possible change of AuCN growth to film formation at high concentrations (Supporting Figure S2). Further study is necessary to fully optimize the device performance and reduce the device-to-device variation. The output curves under different illumination powers also show a typical linear behavior where the observed photocurrent is proportional to the off-current (Supporting Figure S8). This indicates that we can easily achieve higher photoresponsivity by simply increasing the applied drain-source V_{ds} . Previously, the realization of hybrid graphene phototransistors with large UV photoresponsivity has relied on well-known large-gap semiconductors (ZnO and TiO₂).^{29–32} Our study clearly demonstrates that AuCN chains have great potential in optoelectronic applications.

To investigate the doping behaviors of hybrid graphene phototransistors, we changed the power of the incident light and measured the response as shown in Figure 4d. As the power of the incident light increased, we observed a steady shift in the Dirac point to lower values, which indicates the p-doping of graphene is reduced under light illumination. We can draw a band diagram at the AuCN/graphene interface as shown in Figure 4e. With the incident photons, electron-hole pairs were generated in AuCN and electron could be preferentially transferred to graphene due the band bending. Therefore, the p-doping from the original electron-donation from graphene to AuCN is reduced under light illumination, which is consistent with our experimental observation of the Dirac point downshift. The charge transfer under light illumination is more clearly observed under monochromatic light sources as shown in Supporting Figure S9. Interestingly, a feature of new Dirac point was observed at hole transport side (to the negative gate-voltage compared to the original Dirac point) under strong blue and UV illumination. This can be attributed to spatially inhomogeneous charge transfer between AuCN and graphene. The growth of AuCN nanowires on graphene can be spatially nonuniform, which results in the inhomogeneous doping levels in graphene under light illuminations.

The AuCN/graphene phototransistor showed a highly tunable photoresponse depending on the applied gate voltage. As shown in Figure 4b and Supporting Table 1, the hole mobility of AuCN/graphene devices was reduced value under white-light illumination whereas the electron mobility did not significantly change. The device response under white-light illumination is a combination of responses with different wavelengths (Supporting Figure S9) and the apparent reduction of hole mobility can be rationalized. Under negative gate bias conditions, therefore, the effect of reduced hole mobility could be dominant, and we observe a negative photocurrent. On the other hand, when the gate bias was bigger than the Dirac point, a positive photocurrent was observed. The polarity switching of photocurrent from negative to positive is clearly shown in Figure 5a,b. The observed tunability allows us to control the on-off state and gains of the photodetector, which is highly advantageous in the pixelated imaging application. The AuCN/graphene device

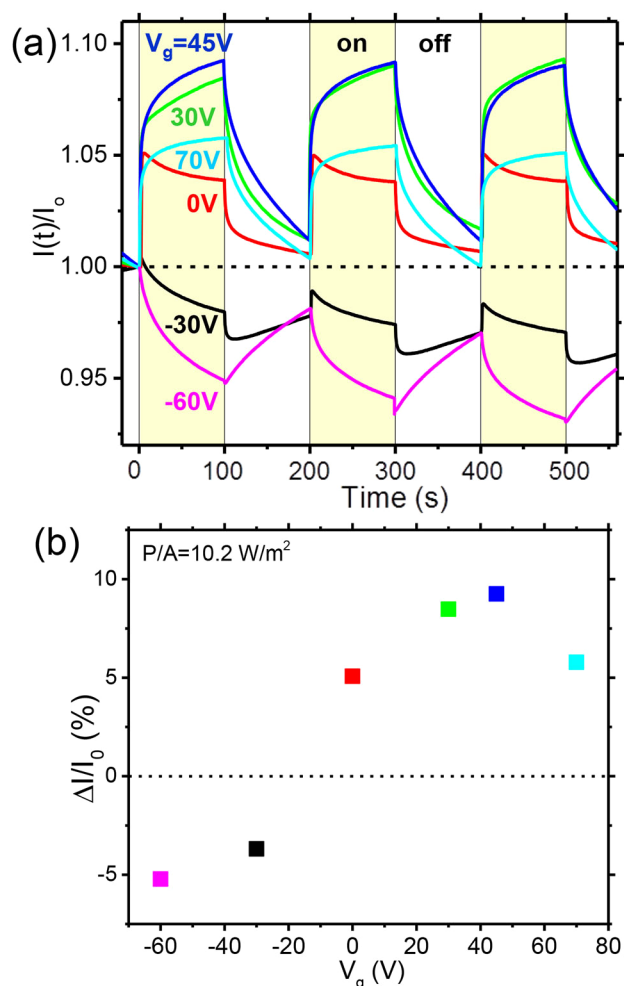


Figure 5. Gate voltage-dependent photoresponse. (a) Gate-voltage-dependent photoswitching characteristics of the AuCN/graphene device under white light illumination (10.2 W/m^2). (b) The normalized photocurrent as a function of gate-voltage change.

also showed good switching behavior under on–off light modulation as shown in Figure 5a. For example, at $V_g = 45 \text{ V}$, the device responding time τ_1 was $\sim 14 \text{ s}$, and decaying response time τ_2 was $\sim 52 \text{ s}$ when fitting to a function of $e^{-t/\tau}$. With intermediate gate bias, such as $V_g = 0 \text{ V}$, we observed the mixing of two opposite photocurrent effects. The response time can be further reduced by removing the induced charge carriers at the interfaces using gate pulsing.^{28,33} With a measured noise level of phototransistors of $\sim 2 \times 10^{-8} \text{ A}/\sqrt{\text{Hz}}$ at $V_g = 0 \text{ V}$ (Supporting Figure S10), we estimated the lowest measurable power density of devices as $\sim 10^{-4} \text{ W/m}^2$ for 3.1 eV photons.

In conclusion, we developed a facile drop-cast method to fabricate epitaxially grown AuCN nanowires on graphene and investigated the evolution of nanowire morphology under different growth conditions. The detailed TEM investigation of AuCN/graphene clearly showed the competition between the diffusion kinetics and energetics during the AuCN nanowire formation process. Using complementary experiments and calculations, we also demonstrated that AuCN is a semiconductor with a bandgap of $\sim 2.7 \text{ eV}$ (direct bandgap value). Moreover, the AuCN/graphene heterostructure showed a prominent photoresponse especially for UV, demonstrating the

potential use of AuCN in optoelectronics. We believe that the family of 1D chain-structured semiconductors^{19,24} can be a crucial component in the fabrication of multifunctional van der Waals heterostructures.

Methods. Graphene Growth. Graphene was synthesized via low-pressure chemical vapor deposition (CVD) on $25 \mu\text{m}$ Cu foil (99.8%, Alfa Aesar).³⁴ The copper foil was inserted into a quartz tube and heated to $1010 \text{ }^\circ\text{C}$ for 30 min under a H_2 flow of 30 sccm at 180 mTorr. After annealing for 30 min, a gas mixture of 30 sccm CH_4 and 30 sccm H_2 at 360 mTorr was introduced for 15 min to grow the graphene. Consequently, fast cooling to room temperature was performed.

Graphene Transfer. Graphene on SiO_2/Si substrates was fabricated using the PMMA-mediated transfer method. For details, PMMA was spin-coated on graphene/Cu foils at 4500 rpm for 50 s. To remove the graphene on the back side of the copper foil, oxygen plasma etching was performed. In order to remove the copper, the PMMA/graphene/Cu stacks were put in a 0.2 M aqueous solution of ammonium persulfate [$(\text{NH}_4)_2\text{S}_2\text{O}_8$] for 12 h. The PMMA/graphene films were rinsed with deionized water three times. Finally, the PMMA/graphene films were transferred onto SiO_2/Si substrates, and then the PMMA films were removed using acetone for 2 h. Graphene TEM grids were fabricated using a direct transfer method without a polymer support.³⁵

AuCN Nanowire Growth. AuCN nanowires were synthesized on the graphene using two different methods. For the first method,²¹ AuCN solution ($1.5 \mu\text{L}$, $0.2\text{--}2.4 \text{ mM}$) was drop-casted on graphene substrates (graphene TEM grid or graphene on SiO_2/Si) using a micropipette. The solution was prepared by dissolving gold cyanide (99.99%, Alfa Aesar) in ammonia solution (14.8 M, Samchun). After the drop-cast, the substrates were heated at $50 \text{ }^\circ\text{C}$ on a hot plate for 15 min. For the second method (incubation method),²⁰ Au nanoparticles (dispersed in organic solvents) were drop-casted and dried on the graphene TEM grids. Then, the samples were floated on an aqueous solution of 0.3 M ammonium persulfate for 10 h and rinsed by transferring the grids to deionized water.

Characterizations. Optical microscope images were acquired using a Leica DM-750 M with visible light. Transmission electron microscopy (TEM) images and selected area electron diffraction patterns (SAED) were obtained with an FEI Tecnai-F20, operated at 200 kV. High-resolution TEM imaging was performed using a spherical aberration (image) corrected FEI Titan G2, operated at 80 kV. Scanning electron microscopy (SEM) images were obtained using FEI-Verios 460L and JEOL IT-500HR at 5 kV. The bandgap of AuCN was determined by UV–vis absorption spectra measurement (Cary 5000 UV–vis–NIR spectrophotometer). For a direct gap transition between the valence and conduction bands, the absorbance A is given as

$$A = \frac{c(h\nu - E_g)^{1/2}}{h\nu} \quad (1)$$

where c is a constant, $h\nu$ is the photon energy, E_g is the optical bandgap energy. The optical bandgap energy was obtained by extrapolating a straight line of the plot $(Ah\nu)^2$ versus $h\nu$.

Device Fabrication and Measurements. The electrodes (Au 100 nm/Ti 5 nm) for the graphene devices were deposited using e-beam evaporation with a metal shadow mask. (Supporting Figure S5) For the hybrid AuCN/graphene device fabrication, AuCN solutions were drop-casted on

graphene devices and dried under mild heating. A parameter analyzer, Keithley 4200, was used to measure the electrical properties of AuCN/graphene devices under $\sim 3 \times 10^{-5}$ Torr at room temperature. Field effect mobility was calculated by

$$\mu = \frac{d_{\text{ox}}}{\epsilon_{\text{ox}}} \times \frac{\Delta I_{\text{ds}}}{\Delta V_{\text{g}}} \times \frac{1}{V_{\text{ds}}} \times \frac{L}{W} \quad (2)$$

where d_{ox} ($= 300$ nm) is the thickness of the SiO_2 layer, ϵ_{ox} is the permittivity of SiO_2 , L and W are the channel length and width, respectively. For a white light source, we used a halogen lamp purchased from Fiber Optic Korea Co., Ltd. The spectrum of the white-light covers wavelengths from 380 to 720 nm. For wavelength-dependent measurements, we used light-emitting diodes purchased from Opto-Edu (Beijing) Co., Ltd. The illumination power to phototransistors was calibrated using a power meter, Thorlabs PM100A. For estimation of the white-light illumination power, the representative wavelength, 574 nm, was used for input to the power meter. We used two kinds of device geometries and the active area of phototransistors was either $45 \mu\text{m} \times 1200 \mu\text{m}$ or $25 \mu\text{m} \times 600 \mu\text{m}$, which was used to calculate the incident illumination power density to phototransistors.

Calculations. Calculations were performed using first-principles method based on the density functional theory.³⁶ We carried out our calculations in the Vienna Ab initio Simulation Package code with a projector-augmented-wave method.³⁷ For the exchange correlation energy functional, the generalized gradient approximation³⁸ was employed in the Perdew–Burke–Ernzerhof scheme, and the kinetic energy cutoff was taken to be 500 eV. To describe AuCN as a bundle packed by the van der Waals interaction, we employed PBE-D2 method using the Grimme's approach.³⁹ The $15 \times 15 \times 15$ k-point sampling was used for the $1 \times 1 \times 1$ AuCN unit cell. Geometry optimization of the structure was carried out until the Hellmann–Feynman force acting on each atom was smaller than 0.01 eV/Å. To obtain accurate energy band gaps, the HSE calculations⁴⁰ were done for the bulk AuCN.

■ ASSOCIATED CONTENT

Supporting Information

The Supporting Information is available free of charge on the ACS Publications website at DOI: 10.1021/acs.nanolett.8b02259.

Additional SEM and TEM images of AuCN/graphene samples depending on the growth conditions, diffuse reflectance of graphene and AuCN/graphene samples, optical images of graphene and AuCN/graphene devices, additional characterizations and data of AuCN/graphene devices under illumination, and a table of field effect mobility of graphene and AuCN/graphene devices (PDF)

■ AUTHOR INFORMATION

Corresponding Author

*E-mail: kpkim@yonsei.ac.kr.

ORCID

Jungwon Park: 0000-0003-2927-4331

Won Chul Lee: 0000-0001-8479-0836

Hoonkyung Lee: 0000-0002-6417-1648

Hu Young Jeong: 0000-0002-5550-5298

Kibog Park: 0000-0003-4086-7365

Kwanpyo Kim: 0000-0001-8497-2330

Author Contributions

J.J. and Y.L. contributed equally to this work. The manuscript was written through contributions of all authors. All authors have given approval to the final version of the manuscript.

Notes

The authors declare no competing financial interest.

■ ACKNOWLEDGMENTS

This work was mainly supported by the Basic Science Research Program through the National Research Foundation of Korea (NRF-2017R1A5A1014862 and NRF-2016R1D1A1B03934008). H.H.Y. and K.P. acknowledge support from the Basic Science Research Program (2016R1A2B4014762) and Global Ph.D. Fellowship Program (2015H1A2A1033714) through the National Research Foundation funded by the Ministry of Science and ICT in Korea. J.S. and J.P. acknowledge support from IBS-R006-D1 and the National Research Foundation of Korea (NRF) grant funded by the Korea Government (MSIT) (NRF-2017R1A5A1015356). S.J. and W.C.L. acknowledge support from the Basic Science Research Program and the Convergence Technology Development Program for Bionic Arm through NRF funded by the Ministry of Science and ICT (2016R1C1B1014940 and 2015M3C1B2052811).

■ REFERENCES

- (1) Geim, A. K.; Grigorieva, I. V. *Nature* **2013**, *499*, 419–425.
- (2) Liu, Y.; Weiss, N. O.; Duan, X.; Cheng, H.-C.; Huang, Y.; Duan, X. *Rev. Mater.* **2016**, *1*, 16042.
- (3) Jariwala, D.; Marks, T. J.; Hersam, M. C. *Nat. Mater.* **2017**, *16*, 170–181.
- (4) Britnell, L.; Ribeiro, R. M.; Eckmann, A.; Jalil, R.; Belle, B. D.; Mishchenko, A.; Kim, Y. J.; Gorbachev, R. V.; Georgiou, T.; Morozov, S. V.; Grigorenko, A. N.; Geim, A. K.; Casiraghi, C.; Neto, A. H. C.; Novoselov, K. S. *Science* **2013**, *340*, 1311–1314.
- (5) Lee, C.-H.; Lee, G.-H.; van der Zande, A. M.; Chen, W.; Li, Y.; Han, M.; Cui, X.; Arefe, G.; Nuckolls, C.; Heinz, T. F.; Guo, J.; Hone, J.; Kim, P. *Nat. Nanotechnol.* **2014**, *9*, 676–681.
- (6) Rivera, P.; Schaibley, J. R.; Jones, A. M.; Ross, J. S.; Wu, S.; Aivazian, G.; Klement, P.; Seyler, K.; Clark, G.; Ghimire, N. J.; Yan, J.; Mandrus, D. G.; Yao, W.; Xu, X. *Nat. Commun.* **2015**, *6*, 6242.
- (7) Massicotte, M.; Schmidt, P.; Vialla, F.; Schädler, K. G.; Reserbat-Plantey, A.; Watanabe, K.; Taniguchi, T.; Tielrooij, K. J.; Koppens, F. H. L. *Nat. Nanotechnol.* **2016**, *11*, 42–46.
- (8) Woods, C. R.; Britnell, L.; Eckmann, A.; Ma, R. S.; Lu, J. C.; Guo, H. M.; Lin, X.; Yu, G. L.; Cao, Y.; Gorbachev, R. V.; Kretinin, A. V.; Park, J.; Ponomarenko, L. A.; Katsnelson, M. I.; Gornostyrev, Y. N.; Watanabe, K.; Taniguchi, T.; Casiraghi, C.; Gao, H. J.; Geim, A. K.; Novoselov, K. S. *Nat. Phys.* **2014**, *10*, 451–456.
- (9) Kim, K.; Coh, S.; Tan, L. Z.; Regan, W.; Yuk, J. M.; Chatterjee, E.; Crommie, M. F.; Cohen, M. L.; Louie, S. G.; Zettl, A. *Phys. Rev. Lett.* **2012**, *108*, 246103.
- (10) Cao, Y.; Fatemi, V.; Fang, S.; Watanabe, K.; Taniguchi, T.; Kaxiras, E.; Jarillo-Herrero, P. *Nature* **2018**, *556*, 43–50.
- (11) Lee, C.-H.; Schiros, T.; Santos, E. J. G.; Kim, B.; Yager, K. G.; Kang, S. J.; Lee, S.; Yu, J.; Watanabe, K.; Taniguchi, T.; Hone, J.; Kaxiras, E.; Nuckolls, C.; Kim, P. *Adv. Mater.* **2014**, *26*, 2812–2817.
- (12) He, D.; Zhang, Y.; Wu, Q.; Xu, R.; Nan, H.; Liu, J.; Yao, J.; Wang, Z.; Yuan, S.; Li, Y.; Shi, Y.; Wang, J.; Ni, Z.; He, L.; Miao, F.; Song, F.; Xu, H.; Watanabe, K.; Taniguchi, T.; Xu, J.-B.; Wang, X. *Nat. Commun.* **2014**, *5*, 5162.
- (13) Liu, X.; Luo, X.; Nan, H.; Guo, H.; Wang, P.; Zhang, L.; Zhou, M.; Yang, Z.; Shi, Y.; Hu, W.; Ni, Z.; Qiu, T.; Yu, Z.; Xu, J.-B.; Wang, X. *Adv. Mater.* **2016**, *28*, 5200–5205.

- (14) Kim, K.; Lee, T. H.; Santos, E. J. G.; Jo, P. S.; Salleo, A.; Nishi, Y.; Bao, Z. *ACS Nano* **2015**, *9*, 5922–5928.
- (15) Lee, T. H.; Kim, K.; Kim, G.; Park, H. J.; Scullion, D.; Shaw, L.; Kim, M.-G.; Gu, X.; Bae, W.-G.; Santos, E. J. G.; Lee, Z.; Shin, H. S.; Nishi, Y.; Bao, Z. *Chem. Mater.* **2017**, *29*, 2341–2347.
- (16) Yang, H.; Heo, J.; Park, S.; Song, H. J.; Seo, D. H.; Byun, K.-E.; Kim, P.; Yoo, I.; Chung, H.-J.; Kim, K. *Science* **2012**, *336*, 1140–1143.
- (17) Tongay, S.; Lemaitre, M.; Miao, X.; Gila, B.; Appleton, B. R.; Hebard, A. F. *Phys. Rev. X* **2012**, *2*, 011002.
- (18) Kim, Y.; Cruz, S. S.; Lee, K.; Alawode, B. O.; Choi, C.; Song, Y.; Johnson, J. M.; Heidelberger, C.; Kong, W.; Choi, S.; Qiao, K.; Almansouri, I.; Fitzgerald, E. A.; Kong, J.; Kolpak, A. M.; Hwang, J.; Kim, J. *Nature* **2017**, *544*, 340–343.
- (19) Bowmaker, G. A.; Kennedy, B. J.; Reid, J. C. *Inorg. Chem.* **1998**, *37*, 3968–3974.
- (20) Lee, W. C.; Kim, K.; Park, J.; Koo, J.; Jeong, H. Y.; Lee, H.; Weitz, D. A.; Zettl, A.; Takeuchi, S. *Nat. Nanotechnol.* **2015**, *10*, 423–428.
- (21) Kim, J.; Lim, K.; Lee, Y.; Kim, J.; Kim, K.; Park, J.; Kim, K.; Lee, W. C. *J. Phys. Chem. Lett.* **2017**, *8*, 1302–1309.
- (22) Zhang, Z.; Lagally, M. G. *Science* **1997**, *276*, 377–383.
- (23) Barth, J. V.; Costantini, G.; Kern, K. *Nature* **2005**, *437*, 671–679.
- (24) Chippindale, A. M.; Hibble, S. J.; Bilbé, E. J.; Marelli, E.; Hannon, A. C.; Allain, C.; Pansu, R.; Hartl, F. *J. Am. Chem. Soc.* **2012**, *134*, 16387–16400.
- (25) Koppens, F. H. L.; Mueller, T.; Avouris, P.; Ferrari, A. C.; Vitiello, M. S.; Polini, M. *Nat. Nanotechnol.* **2014**, *9*, 780–793.
- (26) Li, J.; Niu, L.; Zheng, Z.; Yan, F. *Adv. Mater.* **2014**, *26*, 5239–5273.
- (27) George, P. A.; Strait, J.; Dawlaty, J.; Shivaraman, S.; Chandrashekar, M.; Rana, F.; Spencer, M. G. *Nano Lett.* **2008**, *8*, 4248–4251.
- (28) Konstantatos, G.; Badioli, M.; Gaudreau, L.; Osmond, J.; Bernechea, M.; de Arquer, F. P. G.; Gatti, F.; Koppens, F. H. L. *Nat. Nanotechnol.* **2012**, *7*, 363–368.
- (29) Sun, Z.; Liu, Z.; Li, J.; Tai, G.-a.; Lau, S.-P.; Yan, F. *Adv. Mater.* **2012**, *24*, 5878–5883.
- (30) Guo, W.; Xu, S.; Wu, Z.; Wang, N.; Loy, M. M. T.; Du, S. *Small* **2013**, *9*, 3031–3036.
- (31) Shao, D.; Gao, J.; Chow, P.; Sun, H.; Xin, G.; Sharma, P.; Lian, J.; Koratkar, N. A.; Sawyer, S. *Nano Lett.* **2015**, *15*, 3787–3792.
- (32) Haider, G.; Roy, P.; Chiang, C.-W.; Tan, W.-C.; Liou, Y.-R.; Chang, H.-T.; Liang, C.-T.; Shih, W.-H.; Chen, Y.-F. *Adv. Funct. Mater.* **2016**, *26*, 620–628.
- (33) Roy, K.; Padmanabhan, M.; Goswami, S.; Sai, T. P.; Ramalingam, G.; Raghavan, S.; Ghosh, A. *Nat. Nanotechnol.* **2013**, *8*, 826–830.
- (34) Li, X.; Cai, W.; An, J.; Kim, S.; Nah, J.; Yang, D.; Piner, R.; Velamakanni, A.; Jung, I.; Tutuc, E.; Banerjee, S. K.; Colombo, L.; Ruoff, R. S. *Science* **2009**, *324*, 1312–1314.
- (35) Kim, K.; Lee, Z.; Regan, W.; Kisielowski, C.; Crommie, M. F.; Zettl, A. *ACS Nano* **2011**, *5*, 2142–2146.
- (36) Kohn, W.; Sham, L. J. *Phys. Rev.* **1965**, *140*, A1133–A1138.
- (37) Kresse, G.; Joubert, D. *Phys. Rev. B: Condens. Matter Mater. Phys.* **1999**, *59*, 1758–1775.
- (38) Perdew, J. P.; Burke, K.; Ernzerhof, M. *Phys. Rev. Lett.* **1996**, *77*, 3865–3868.
- (39) Grimme, S. *J. Comput. Chem.* **2006**, *27*, 1787–1799.
- (40) Heyd, J.; Scuseria, G. E.; Ernzerhof, M. *J. Chem. Phys.* **2003**, *118*, 8207–8215.